Green Chemistry

PAPER

View Article Online
View Journal | View Issue

Cite this: *Green Chem.*, 2024, **26**, 10196

Green synthesis of sodium pyrithione salt-activated biomass-derived carbon for aqueous zinc-ion capacitors†

Lingqi Huang,[a,b] Zilong Gu,[a] Jiayang Gu,[a] Fei Zhang, *[c,f] Jingshun Zhuang,[a] Qingzhi Ma,[a] Tao Zhang,[d] Jingfei Li,[e] Heyang Liu *[a,d] and Wei Feng *[b]

Conversion of biomass into doped activated carbons (ACs) *via* green processes is envisioned as a promising path toward modern energy storage applications. ACs are commonly synthesized using strong bases, which are associated with environment and operation risks. Thus, it is necessary to find alternative and green activation reagents. Herein, we report a multi-functional molecular salt (sodium pyrithione) as an activation reagent for the economically viable preparation of doped ACs with a large surface area, rich dopants, and porous structures. The formation of carbons and the variation in the composition and pore architecture were demonstrated. The prepared ACs were then fabricated into cathodes for a zinc-ion capacitor. We correlated the properties of ACs with their performance by analyzing electrochemical measurements. Meanwhile, the optimal SPHC-based ZIC delivered high capacity and excellent cycling stability over 20 000 cycles under practical conditions. Moreover, we found that long-term chemical adsorption/desorption on active sites of ACs influences the cathode structure and thus leads to a loss of capacity and changes in the energy storage mechanism. Overall, this work provides an alternative protocol for the synthesis of doped ACs, which can be used as cathodes materials for practical high-performance ZICs.

Received 17th May 2024,
Accepted 11th July 2024

DOI: 10.1039/d4gc02429j

rsc.li/greenchem

1. Introduction

Activated carbons (ACs) are abundant and versatile materials consisting of randomly stacked imperfect thin graphite layers that enclose numerous interconnected holes.[1] The high degree of tunability of synthetic topologies affords ACs with large surface areas and hierarchical pore distributions, making ACs promising candidates for practical cathode materials for hybrid-type zinc-ion capacitors (ZICs). The intriguing surface area and porosity allow for high power cathodes by accommodating fast charge adsorption/desorption storage mechanisms at the surface of ACs.[2,3] In addition, the defective carbon backbone structure can be functionalized by inserting a variety of doped atoms at defect sites and/or edges, affording surface faradaic reactions and enhanced electrochemical performance in the cathodes.[4–6] At present, considerable research has been devoted to the delicate optimization of the pore architecture, surface area, dopants, *etc.*,[7,8] aiming for performance-balanced ACs for high-energy and high-power ZICs.

The traditional route for the synthesis of doped ACs involves high-temperature treatment of pristine carbons with activation reagents and modifiers, but this often requires pristine carbon materials obtained from the pyrolysis of agricultural feed-stocks or certain petroleum-derived products (Scheme 1a).[9] Moreover, the treatments commonly involve the use of corrosive activation reagents, organic doping reagents, multiple elevated temperatures, long reaction times, *etc.*[10–12] For example, Ye *et al.* developed highly porous carbon spheres for battery application, where the carbons were first prepared through catalytic emulsion polymerization using expensive diethynylbenzenes, followed by hydrothermal treatment and activation steps with large amounts of KOH.[13,14] Qiu *et al.* modified the pyrolysis process of lignin by introducing alkali moieties and triazine-based supermolecules in a two-step and

[a]School of Environmental and Natural Resources, Zhejiang University of Science and Technology, Hangzhou, 310023, P. R. China. E-mail: heyang.liu@zust.edu.cn
[b]School of Materials Science and Engineering, Tianjin University, Tianjin, 300072, P. R. China. E-mail: weifeng@tju.edu.cn
[c]Leibniz-Institut für Polymerforschung Dresden e.V. (IPF), Hohe Str. 6, 01069 Dresden, Germany. E-mail: feizhang@tju.edu.cn
[d]School of Biological & Chemical Engineering, Zhejiang University of Science and Technology, Hangzhou, 310023, P. R. China
[e]Zhejiang Institute of Quality Sciences, Hangzhou, 31000, P. R. China
[f]School of Science and Engineering, The Chinese University of Hong Kong, Shenzhen, Shenzhen, Guangdong 518172, P. R. China

†Electronic supplementary information (ESI) available. See DOI: https://doi.org/10.1039/d4gc02429j

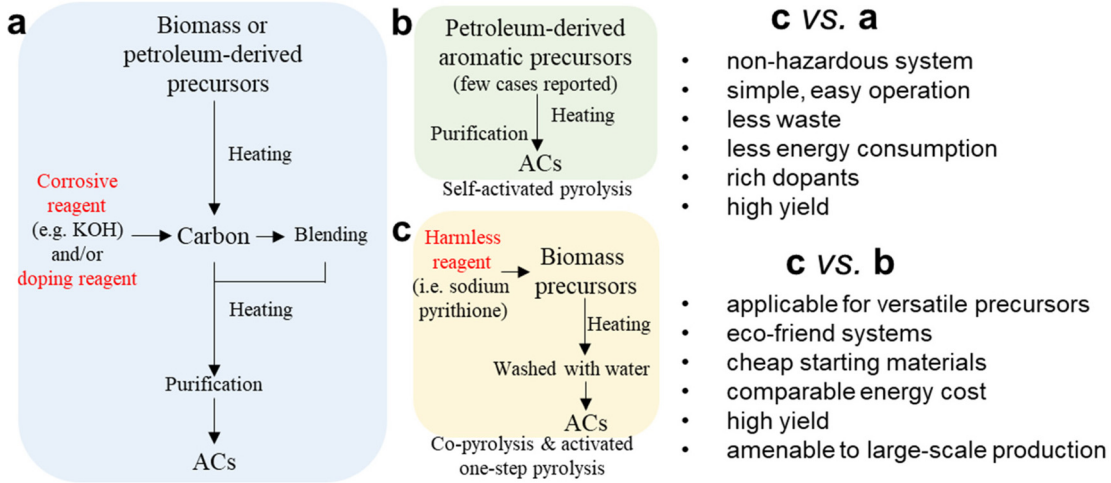

Scheme 1 Synthesis steps for doped ACs.

slow-heating procedure, which results in the synthesis of high nitrogen-doped carbon for potassium storage application.[15] Shen *et al.* prepared dual-doped ACs using a three-step procedure comprising biochar preparation, KOH activation, and post-treatment with thiourea.[16] Regarding practical production conditions, it is highly desirable to avoid the use of hazardous chemicals that exhibit toxicity and pose risk to human health and the environment. Moreover, burdensome processes that require more energy/source input and produce more waste should be avoided when proposing replacement protocols.[17] The increasing attention directed toward sustainability from the natural sciences provides incentives to create alternatives to hazardous substances and develop new routes for doped ACs.

Self-activated pyrolysis is an alternative green and sustainable route for the preparation of doped ACs (Scheme 1b). The route can be simple and effective because the carbon texture formation, pore generation, and heterogeneous atom insertion occur within the one-step elevated temperature with the use of specific precursors. For example, Alshareef *et al.* prepared oxygen-rich ACs by pyrolysis of pyromellitic acid tetrapotassium salt, where the benzene ring, carbonyl group, and potassium work as the carbon source, dopant, and pore generate agent, respectively.[2] Similarly, other precursors (such as tetra-alkali metal pyromellitic acid,[18] potassium phthalimide,[19] and sodium polyacrylate)[20] have been recently reported with applicability in the synthesis of advanced doped ACs with the one-step protocol. Similar pyrolysis mechanisms have been demonstrated. Moreover, such protocol eliminates the use of hazardous reagents and reduces burdensome heating processes, allowing for the greener and low energy-demanding production of doped ACs materials. However, such precursors are rare; the prices are higher than common biomass, feed-stocks, or petroleum-derived products; and they often afford limited carbon yields. Engineered co-pyrolysis is another promising route for doped ACs, involving the use of carbonaceous matter and reagents. For example, N/S co-doped porous carbon was synthesized by co-pyrolysis of sodium lignosulfonate and melamine.[21] N, O, and F tri-doped porous carbon with a large surface area of carbon (>3000 m^2 g^{-1}) was prepared by co-pyrolysis of two powder organic monomers and KOH chips in one batch.[22] One advantage of co-pyrolysis is that the post-activation and doping process can be eliminated. Additionally, the required chemicals and materials are versatile, easy to use, cheap, and amenable to large-scale production.

Lignin and hemicellulose are biomass sources mainly composed of carbohydrate units, but exhibit three-dimensional polymer structures and interwoven molecular architectures.[23,24] Owing to their attractive structural properties, they have been demonstrated to be appropriate precursors for ACs, and subsequently employed as adsorbers,[25] electrode materials,[26] anode materials in batteries,[27] cathode materials in capacitors,[28] *etc*. The utility of lignin and hemicellulose for doped ACs has been extensively investigated due to their merits of being low-cost, renewable, environmentally friendly, and having scale-up potential, *etc*.[5] Nevertheless, traditional treatments and procedures are still the prerequisites. In this work, we sought to develop an alternative green and sustainable route for the preparation of doped ACs *via* co-pyrolysis of lignin or hemi-lignin in the presence of sodium pyrithione, which is a commercially available cheap ($2–$4 per kg), harmless molecular salt, consisting of N, S, O heteroatoms and Na for self-activation. The proposed process is simple, green, safe, and economical, compared to existing methods (Scheme 1c). Meanwhile, the resultant biomass-derived doped ACs show high surface areas (~1218 m^2 g^{-1}) and are heteroatom-rich. Accordingly, ZICs assembled with biomass-derived doped ACs delivered the highest reversible capacity of 108.6 mA h g^{-1} and energy density of 67.8 W h kg^{-1} in aqueous ZIC systems, outperforming traditional ACs that were synthesized with hazardous NaOH. Moreover, the cathodes also displayed excellent cycling stability during the 20 000-charge–discharge measurement, indicating its great potential in ZIC application.

2. Experiments

2.1 Materials

Crude enzymatic lignin was provided by Shandong Longlive Bio-technology Co., Ltd, and was used without purification. Poplar hemicellulose was prepared after basic hydrolysis, membrane separation, and spray drying procedures. Sodium pyrithione (SP, 96%), sodium hydroxide (SH, 96%), $ZnSO_4 \cdot 7H_2O$ (AR, 99%), *N*-methyl-2-pyrrolidinone (NMP, 99%), poly(vinylidene fluorideco-hexafluoropropylene) (PVDF-HFP, Lot#P875306), carbon black (Cabot vulcan XC-72), and Zinc foil (0.25 mm, 99.99%) were purchased from Shanghai Macklin Biochemical Technology Co., Ltd.

2.2 Preparation of biomass-derived carbon

Enzymatic lignin or hemicellulose was weighted into a nickel boat for direct pyrolysis. The system was first vacuumed and purged with nitrogen gas in triplicate prior to heating. Afterwards, a consistent nitrogen flow of 10 mL min^{-1} and a ramping rate of 5 °C min^{-1} were applied. The biomass was eventually treated at 800 °C for one hour for the formation of carbon materials. The solid char was washed with HCl and water for 2 days to remove possible salt or impurities derived from the biomass itself. After simple drying at 60 °C for 8 h, the products LC or HC were obtained.

2.3 Preparation of biomass-derived activated carbon

Enzymatic lignin or hemicellulose was mixed with the traditional activation reagent sodium hydroxide (SH) or sodium pyrithione (SP) for the preparation of ACs. Equal amounts of biomass and SH or SP were weighed into a nickel boat for pyrolysis under exactly the same procedures. The generated char was washed with HCl and water carefully to remove all sodium compounds and impurities. After drying, lignin-derived products (SHLC and SPLC) and hemicellulose-derived products (SHHC and SPHC) can be obtained. The detailed pyrolysis condition is presented in Table S1.†

2.4 Characterization

The thermal stability of raw materials was evaluated using a TA Discovery Sdt 650, with a heating rate of 20 °C min^{-1} (50–800 °C) in a nitrogen atmosphere. The Fourier transform infrared spectra (FTIR) of biomass was obtained from a TENSOR II FTIR Routine Spectrometer. The morphology and energy-dispersive X-ray spectroscopy (EDX) mapping of carbon materials were characterized by field emission scanning electron microscope (SEM, TESCAN Mira3, Hitachi SU1510). Their surface area and pore distribution were analyzed with an ASAP2460 from Micromeritics, using nitrogen gas as the adsorbate. The surface composition of carbons was analyzed with an X-ray photoelectron spectrometer (Thermo Scientific K-Alpha$^+$ XPS). The phase structure of the carbons was characterized by an X-ray diffractometer (Rigaku Smartlab, equipped with a D/tex Ultra 250 detector) and a Raman spectrometer (Renishaw Invia microscopy system with a 515 nm laser).

2.5 Electrochemical measurements

The as-prepared carbon materials, carbon black and PVDF-HFP (solution in NMP) were mixed for 2 days at a fixed weight ratio of 0.85 : 0.10 : 0.05. The dispersions were then cast onto pieces of carbon papers for practical cathode application in ZICs. The loading amounts were determined by differential weighting method prior to assembling with zinc foil in 2 M $ZnSO_4$ aqueous electrolyte. Gravimetric charge/discharge (GCD) and cyclic voltammetry (CV) measurements were all conducted in a voltage window of 0.2–1.8 V. The electrochemical impedance spectroscopy (EIS) curves were measured *vs.* frequency at ~1.2 V and 0.005 V amplitude. The capacity (C, mA h g^{-1}) and energy density (E, W h kg^{-1}) of ZICs were calculated from GCD measurements, according to the literature equations.[22] The capacitive contribution ratios were calculated from CV results based on Dunn's method.[29]

3. Results and discussion

The morphology and chemical composition of raw materials were first characterized prior to pyrolysis process. In Fig. S1,† lignin displays chunks of amorphous character, while hemicellulose exhibits spherical shapes with surface wrinkle features, which were caused by spray drying. The FTIR spectra of lignin and hemicellulose shown in Fig. S2a† were assigned according to literature. The broad absorption peak at ~2930 cm^{-1} represents the stretching vibration of methyl and methylene groups in lignin, and the peaks at ~1700 and ~1420 cm^{-1} represent the conjugated carbonyl groups and phenols, respectively.[30] The peaks at 3190 and 3670 cm^{-1} can be explained mainly by the presence of hydrophilic functionalities, and the peak at 1475 cm^{-1} represents the deformation stretching of methylene and methine groups in hemicellulose.[31,32] In Fig. S2b,† the XRD characterization indicates the amorphous structure in lignin and the partial crystalline structure (cellulose I) in hemicellulose.[33,34] Fig. S2c† presents the thermal gravimetrical analysis (TGA). Lignin contains a supermolecule network structure and huge amounts of aromatic-containing units that are relatively pyrolysis-inert, and thus produces a dense carbon skeleton after high-temperature treatment.[35] Hemicellulose is composed of xylose units. The existing huge amounts of oxygen-containing groups tend to be eliminated and give a porous carbon skeleton during the pyrolysis process.[36] Additionally, the typical weight loss in the temperature range of 230–330 °C is mainly caused by the degradation of polysaccharide moieties.[37] The results demonstrate high char yield values of 37% and 27% for LC and HC at 800 °C, respectively, indicating the great potential for the preparation of carbon materials.

Fig. 1a & d shows the SEM images of lignin and hemicellulose-derived carbon materials (LC and HC) without the use of any other regents. The morphologies were inherited from their precursors (Fig. S1†). The pyrolysis allows char yields of 35% and 19% for LC and HC, respectively (Table S1†). Compared to the TGA result, the reduced yield was

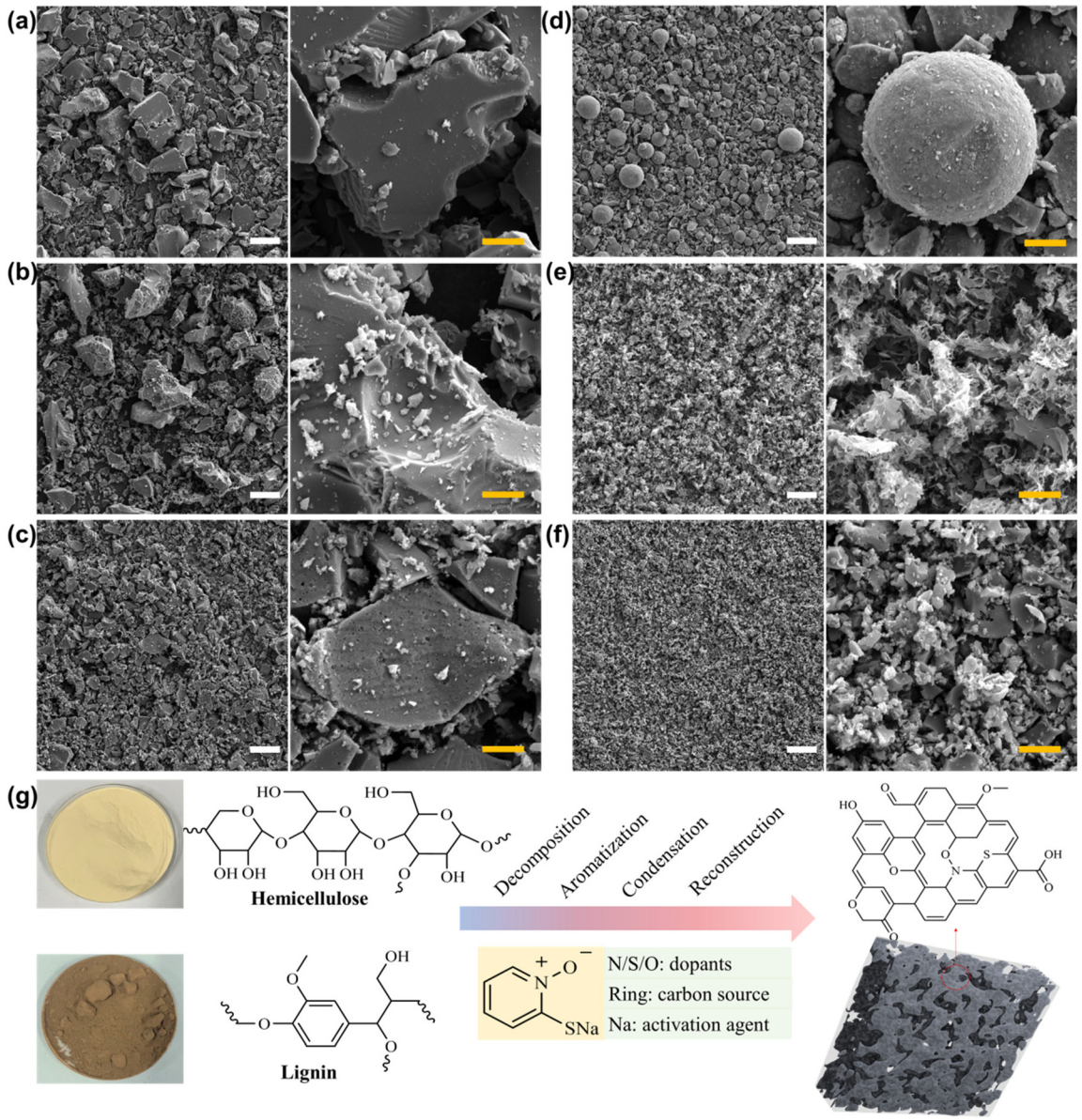

Fig. 1 SEM images of lignin and hemicellulose-derived carbon materials at different magnifications: (a) LC, (b) SHLC, (c) SPLC, (d) HC, (e) SHHC, and (f) SPHC, (white bar: 50 μm, yellow bar: 10 μm). (g) Schematic of the possible SP-derived carbon formation pathway.

attributed to one hour of extended pyrolysis at 800 °C. However, the produced carbons show limited surface areas of 2.2 and 6.6 $m^2 g^{-1}$ for LC and HC, respectively. The heterogeneity of the surface area is affected by the composition and pyrolysis condition. With the used pyrolysis condition, elimination of functional groups and the release of small molecules are insufficient for the formation of a highly porous architecture and large surface area. In the following, the biomass was pyrolyzed with the help of NaOH (Fig. 1b & e) and SP (Fig. 1c & f). Visibly, these particles are broken down into smaller pieces with concave features and microcavities on the surface of the produced activated carbons (ACs). The obvious changes are due to the activation process, which also suggests that SP would etch the carbon skeleton under the same pyrolysis condition (Fig. 1g). Compared to hemicellulose-derived carbon (Fig. 1e & f), the morphologies of the lignin-derived carbon (Fig. 1b & c) are nearly unchanged, which is mostly due to the relatively robust carbon skeleton.

The traditional NaOH acts as a strong oxidizing agent at high temperature, promoting the removal of carbon atoms and the development of nanocavities. However, it is a highly corrosive and would generate a high level of heat as it dissolves during the pre-treatment and post-treatment procedure. Moreover, the strong base could induce chain breaking for lignin and hemicellulose, and lead to an incapability to control the pyrolysis. Fig. S3† shows the characteristics of the biomass and their aqueous mixtures. The NaOH-catalyzed cleavage of aryl ether bonds in both lignin and hemicellulose

leads to chain scission, improved water solubility, enhanced viscosity, and darkened color.[38] Additionally, the mixing of the precursor and a strong base produces extreme heat (~70 °C), and could induce high operation risk. In contrast, the mixing of the precursor and SP molecular salt leads to almost no heat (~25 °C) and allows for safe pre-treatment. Moreover, the chain scission of biomass might not occur as the viscosity of the mixture merely changed. Such behavior makes SP an effective and harmless reagent in producing microporous carbons.

Based on the nitrogen adsorption and desorption isotherms in Fig. 2a, the surface areas of SHLC, SHHC, SPLC and SPHC are calculated to be 374.8, 405.3, 249, and 1217.9 $m^2 g^{-1}$, respectively (Table S1†). Although typical type IV hysteresis features have been observed, the four carbons are micropore-dominated, conferring to the pore distribution curves (Fig. 2b). The skeleton structure and composition of porous carbon are also essential for the electrochemical performance. In Fig. 2c, all carbons exhibit two broad characteristic peaks centered at ~23.1° and ~45°, which are attributed to the [002] and [100] planes of the carbon skeleton structure.[39] The result demonstrates the amorphous disorder of the carbons with large amounts of defects. In Fig. 2d, the D band (~1350 cm^{-1}) and G band (~1590 cm^{-1}) are presented, ascribed to the defective graphitic structure and packed graphitic layers, respectively.[40] The ratios of I_D/I_G are calculated based on the peak intensities, which reflect the defects and disordered structures in the porous carbon. All carbons show I_D/I_G in the range of 0.8–0.84. Considering that cellulose chains experience more severe thermal cleavage and elimination of pyranose rings, this contributes to the aromatic condensation and slightly enhanced long-range stacking in the hemicellulose-derived carbon (HC). The addition of NaOH and SP induce further reactions at high temperature, and thus leads to more defects and disordered structures. The high level of aromaticity in lignin contributes to the resistance to thermal cleavage, requiring more energy for the preferential formation of the stacking structure and structure arrangement.[40] It could be understandable that the addition of activation reagents results in a smaller effect on the defects of the lignin-derived carbons.

The dopants can promote the adsorption of the electrolytes and provide extra pseudocapacitive reactions, and thus lead to favorable electrochemical kinetics and performance.[41] All biomass and mixtures allow the formation of oxygen-doped ACs after the pyrolysis process (Fig. 2e). This is due to the presence of rich oxygen-containing functionalities. Moreover, SPLC and SPHC carbons show extra nitrogen dopants that were inherited from SP molecules (Fig. 2f and Table S1†). Herein, the cyclic and conjugated SP molecules not only act as an activation reagent, but also as a source of carbon skeleton building block. The TGA curve reveals that SP has a high sublimation temperature and high retention (>40 wt%) at 800 °C (Fig. S2c†). Therefore, it is proposed that SP could fuse with degraded biomass species at the aromatization stage during the co-pyrolysis process, rendering the randomly stacked doped graphite layers. Meanwhile, the sodium counter-ions decomposed into sodium species, which activated the graphite layer and create microcavities and defect structures. To further investigate the composition, SP was mixed with an equal mass of SPLC or SPHC for a second co-pyrolysis. It is found that the additional SP treatment in both cases apparently increases the surface nitrogen and sulfur contents (Fig. S4 and Table S1†).

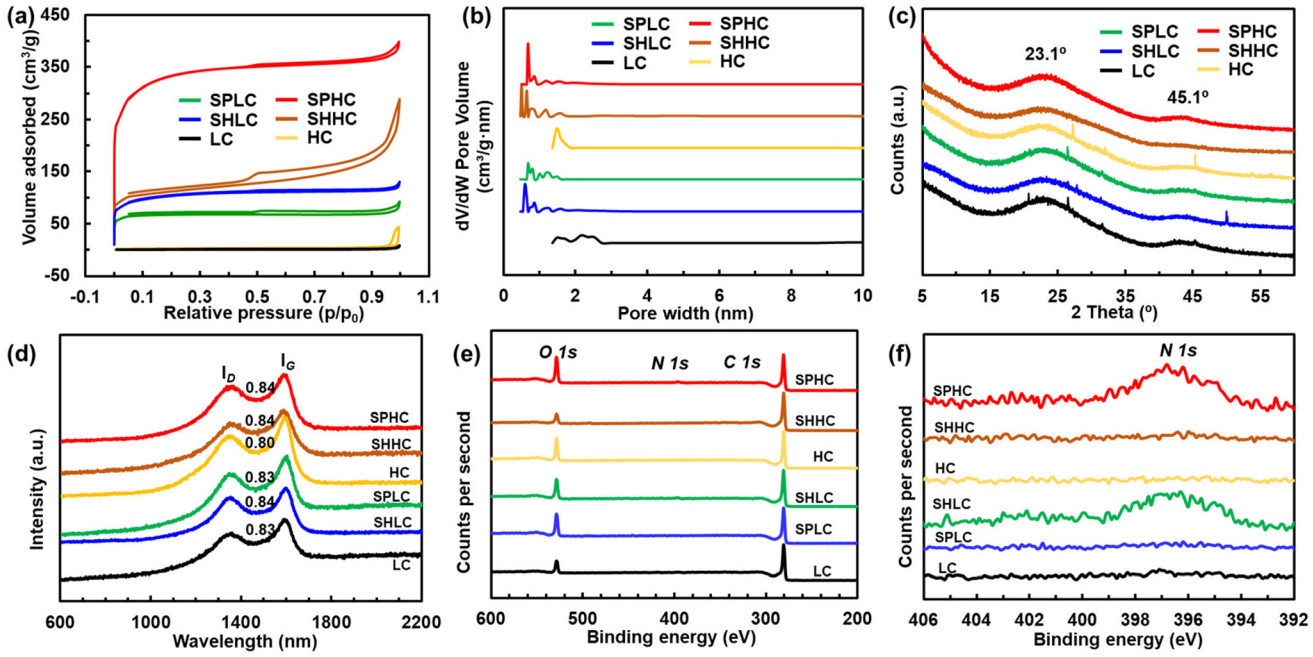

Fig. 2 (a) Nitrogen isotherms, (b) pore distributions, (c) XRD patterns, (d) Raman spectra, (e) XPS survey curves, and (f) high-resolution N 1s spectra of the produced carbons.

The result indicates that the doping mechanism is also applicable to carbon. Additional treatment of SPLC or SPHC with the SP molecular salt further influences the defects and carbon structures, as evidenced from the increased I_D/I_G ratios and shifted [002] planes (Fig. S5†). However, the high-temperature fusing of SP derivatives with microporous carbon blocks the micropores, and leads to decreased surface areas of ACs (Fig. S6†).

Next, carbon cathodes were prepared and assembled into ZICs for electrochemical analysis. Fig. 3a and Fig. S7† show the cyclic voltammetry (CV) profiles of ZICs measured in 2 M aqueous $ZnSO_4$. The cathodes show approximate rectangular shapes with a few redox bumps, indicating the feature of the electric double-layer capacitive behavior and the presence of surface faradaic behavior. Moderate good rate performance can be achieved because satisfactory shapes are retained at faster scan rates (Fig. S7†). Among those cathodes, LC and HC cathodes show extremely small CV areas due to limited surface areas. The SPHC cathode shows the largest area at the same scanning rate, ascribed to the large surface area and heteroatoms. However, it is found that the enhanced heteroatoms but with reduced surface areas render the cathodes (SP2LC and SP2HC) with inferior electrochemical performance (Fig. S7†). Thus, more calculations and measurements are conducted to comprehend the best performance of the SPHC cathode. In Fig. 3b, the intrinsic kinetics of the carbon cathodes is analyzed based on CV profiles using Dunn's method.[29] The capacitive contributions continually increase with the increase of scan rates. It is also noted that NaOH-activated carbon cathodes show an overall larger capacitive performance compared to the SP-activated carbon cathodes. It is believed that co-pyrolysis of SP and biomass provides oxygen/nitrogen/sulfur dopants and tortuous pathways at the same time, which restricts the rate of charge transportation. Nevertheless, SPHC shows relatively good capacitive contribution of 45%, 48%, 55%, and 79% at scan rates of 5, 10, 25, and 100 mV s^{-1}, respectively. The results suggest the fast kinetics and redox process in the SPHC cathode.

Galvanostatic charge–discharge (GCD) measurements have also been carried out (Fig. S8†). The profiles at different current densities exhibit nearly triangular shapes, supporting its good electric double-layer characteristic. Fig. 3c shows the derived voltage-capacity profiles of four ACs at 1 A g^{-1}. SPHC delivers a high capacity of 94.9 mA h g^{-1}, beyond that of SHHC (51.2 mA h g^{-1}), SPLC (44.2 mA h g^{-1}), and SHLC (39.1 mA h g^{-1}), at the same current density. The performance of SPHC is comparable to most reported studies, ZnLFK-PC,[28] AC,[42] CSMCs,[43] N-HPC,[44] *etc*. Fig. 3d presents the rate performance in the current densities of 0.5–10 A g^{-1}. SPHC has a favorable capacity retention of 45.8%, which is higher than that of SHHC (39.8%), SPLC (24.4%), and SHLC (30.7%). Besides, the highest capacity of 108.6 mA g^{-1} is achieved on the SPHC cathode at a lower current density of 0.5 A g^{-1}, ensuring the highest energy density of 67.8 W h kg^{-1} (Fig. 3e). Owing to the high surface area and suitable dopants, SPHC possesses excellent electrochemical performance. Electrochemical impedance spectroscopy (EIS) technique has been used to illustrate the resistance properties of the cathodes. The Nyquist plots first demonstrate that all cathodes experience small, similar electrode resistances (10–12.5 Ω) (Fig. 3f). At high frequencies, the electrolyte resistance values are determined to be about 40 Ω, 85 Ω, 90 Ω, and 135 Ω for SPHC, SHHC, SPLC, and SHLC,

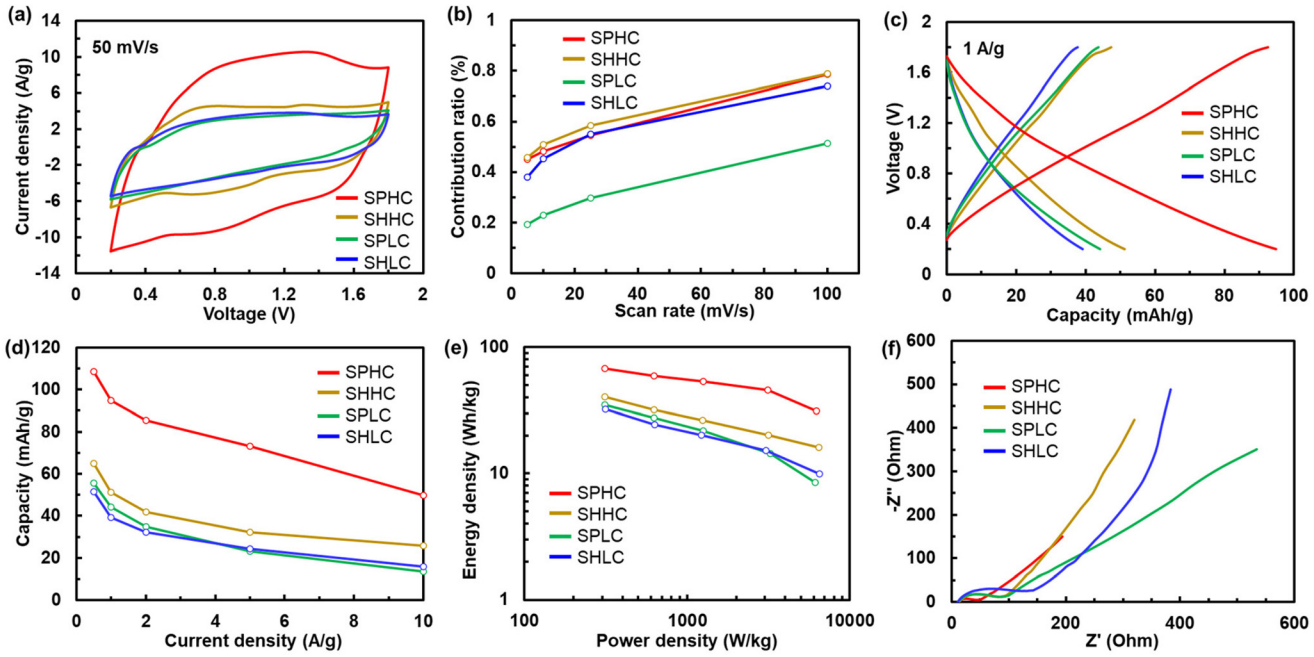

Fig. 3 Electrochemical analysis of ACs: (a) CV curves at 50 mV s^{-1}, (b) capacitive contribution in cathodes at different scan rates, (c) CD profiles at 1 A g^{-1}, (d) rate performance at different current densities, (e) Ragone plots, and (f) Nyquist plots.

respectively. The SP-derived ACs show smaller electrolyte resistance compared to the NaOH-derived ACs. Although the pack structure of cathode influences the resistance, it is believed that the oxygen/nitrogen/sulfur dopants lower the surface energy and enhance the surface electrolyte wettability, resulting in smaller interfacial resistance.[28] Meanwhile, the dopants and tortuous pathways associated with SP-derived ACs affect the charge diffusion and capacitive behavior, resulting in slow slopes or more Warburg-like feature at medium frequencies. The resistance properties agree well with their electrochemical properties and certify the well-performed SPHC cathode.

Fig. 4adisplays the cycling performance of SPHC-based ZIC. To better investigate the electrochemical behavior on the SPHC cathode, zinc foils are often replaced to exclude the influence of the anode on ZIC. Moreover, the cycling measurement was paused randomly for 25 times (~250 h of total break time) and ran under fluctuating temperatures to record the result that mimics practical use condition. As a result, after 20 000 cycles at 7 A g^{-1} (~280 h), the device still maintains a high-capacity retention of 85.9% and nearly ~100% coulombic efficiency, demonstrating excellent cycling stability. Moreover, it is noted that the temperature shows a positive correlation effect on the capacity retention. This is possibly due to the enhanced charge transport at elevated temperatures. After cycling, the resistance property was evaluated by EIS (Fig. 4b). The electrode resistance and electrolyte resistance increase from 10 Ω to 17.8 Ω and from 40 Ω to 73.7 Ω, respectively, whereas the Warburg-like feature remains close. Evidences exist on the dynamic performance of the SPHC cathode on ZIC, despite the electrode structure being supposedly stable at the conducted electrochemical condition. The occurrence of the faradaic redox reaction, electrolyte, and the effect of temperature fluctuation could be considered to play a role in the cathode structure reconstruction,[22] leading to the reduced capacity retention. The self-discharge performance describes the long-term charge storage properties of the ZIC. In Fig. S9,† the open-circuit voltage of SPHC-ZIC has been monitored. Although the voltage drops rapidly from 1.80 V to 1.44 V during the first 20 h, high voltage retention values (~1.38 V) have been observed during the next 100 h. The slow self-discharge rate is comparable with reported work,[45] and the result demonstrates the superior anti-self-discharge performance.

Morphologic and elemental analyses were performed on the SPHC cathodes, and the results are presented in Fig. 4(c–e). Generally, discharging from a high voltage to low voltage would lead to the formation of a zinc complex. Therefore, this will increase the Zn species on the surface of the cathode. Upon charging, the reverse process occurs. The H^+ ions are

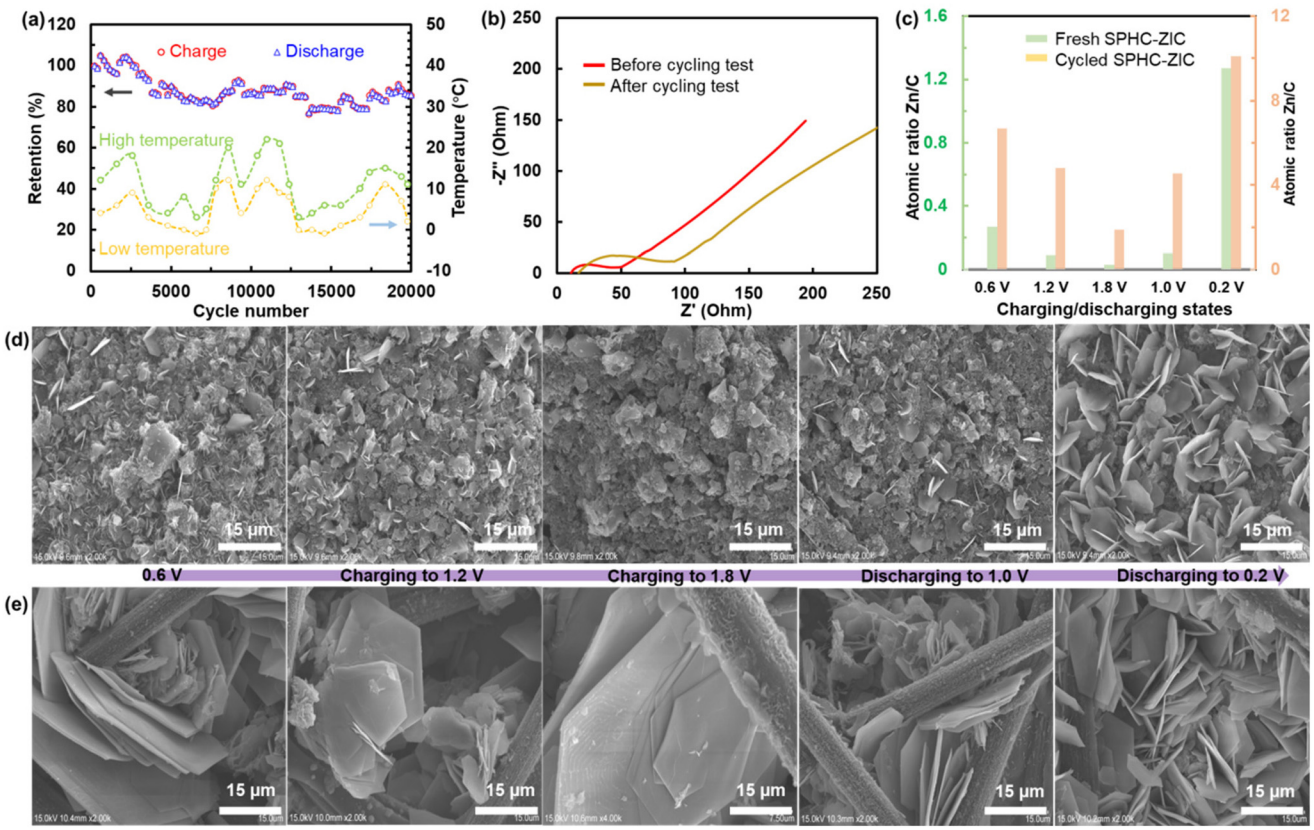

Fig. 4 (a) Cycling measurement performed on a SPHC cathode-based ZIC at ambient condition at 7 A g^{-1}. (b) EIS profiles before and after the cycling test. (c) Atomic ratio of Zn/C at different voltages during the charging process. Images of the (d) fresh SPHC cathode and (e) cycled SPHC cathode at different states.

proposed as the major intermediates for cathode reconstruction *via* precipitation-redissolution of complex zinc hydroxides.[22,46,47] Here, the *operando* techniques experimentally confirm the electrochemical process and mechanism. In Fig. 4c, the EDX quantitative analysis on the fresh SPHC cathode first shows the decrease of the Zn/C ratios (from 0.27 to 0.09, and to 0.03) and then shows the increase of Zn/C ratios (from 0.03 to 0.10 and to 1.27) during charging and discharging. Accordingly, in Fig. 4d, the gradual dissolution and then reformation of the zinc complex during charging and discharging have been identified. Although the cycled SPHC cathode displays the same mechanism, *i.e.*, the Zn/C ratios decrease from 6.69 to 4.79 and to 1.86 upon charging and the ratios increase from 1.86 to 4.56 and to 10.11 upon discharging, the ratios are extraordinarily high. In particular, the Zn/C ratio at 1.8 V is much higher than 0, indicating the presence of a large quantity of the Zn species. This also means that the intermediates do not react stoichiometrically. The feature can also be recognized from the morphologies shown in Fig. 4e, where large zinc complex-based flakes exist at all states (including the state at 1.8 V). Partial degradation of the surface-active functionalities under long-term electrochemical measurement leads to an inequivalent stoichiometric reaction between the intermediates and electrolyte. Therefore, the flakes reside on the cathode at 1.8 V.[48] Moreover, it is believed that the numerous crystal precipitation-redissolving repeats drive the reconstruction of the cathode structure, possibly by modifying the original configurations, breaking the conductive junctions, engulfing the active sites, blocking cavities, *etc.*,[48,49] thus resulting in the capacity loss during cycling.

4. Conclusions

Hemicellulose or lignin has been pyrolyzed in the presence of activation reagents in order to obtain ACs for ZIC application. The cheap, mild, and non-hazardous sodium pyrithione (SP) has been selected as the activation reagent during pyrolysis, in comparison with the traditional NaOH reagents. The derived ACs show porous architectures and multi-dopants, whereas SPHC shows the highest surface area (~1218 $m^2 g^{-1}$) among the four ACs. Based on the archived physiochemical results, SP enables the preparation of novel biomass-derived ACs due to the existence of the oxygen/nitrogen/sulfur groups, ring structure, and sodium ions. Herein, the SP molecules act as dopants, carbon sources, and self-activation reagent, respectively. During ZIC operation, the SP-activated ACs show superior energy storage performance over the NaOH-activated ACs. The SPHC-ZIC delivers high capacity and energy density, excellent cyclability, and admirable anti-discharge performance. Furthermore, the elemental and morphological analysis on the fresh and cycled SPHC cathodes reveal the mechanism of energy storage and retention loss. The proposed SP molecules are a promising reagent for the preparation of high-performance porous carbon towards practical ZIC application. This work also motivates the development of biomass-derived carbons and novel doped porous carbons, and encourages research efforts on electrochemical applications.

Data availability

The data supporting this article have been included as part of the ESI.†

Conflicts of interest

The authors declare that they have no known competing financial interests or personal relationships that could have appeared to influence the work reported in this paper.

Acknowledgements

We are grateful for the financial support from the Zhejiang Provincial Key Research and Development Program (Grant No. 2024C01204 and No. 2024C01240(SD2)), the National Natural Science Foundation of China (Grant No. 52203103 and No. 52327802), Innovation Research Project for Youth Scholar of School of Environment and Natural Resources, Zhejiang University of Science and Technology (HZQY202403) and the University Affair Basic Grant (2023QN113).

References

1 Y. W. Zhu, S. Murali, M. D. Stoller, K. J. Ganesh, W. W. Cai, P. J. Ferreira, A. Pirkle, R. M. Wallace, K. A. Cychosz, M. Thommes, D. Su, E. A. Stach and R. S. Ruoff, *Science*, 2021, **332**, 1537–1541.
2 J. Yin, W. L. Zhang, W. X. Wang, N. A. Alhebshi, N. Salah and H. N. Alshareef, *Adv. Energy Mater.*, 2020, **10**, 2001705.
3 H. Y. Wang, W. Q. Ye, Y. Yang, Y. J. Zhong and Y. Hu, *Nano Energy*, 2021, **85**, 105942.
4 T. Wang, X. B. Zang, X. M. Z. Wang, X. X. Gu, Q. G. Shao and N. Cao, *Energy Storage Mater.*, 2020, **30**, 367–384.
5 G. B. Lou, G. Pei, Y. T. Wu, Y. Z. Lu, Y. T. Wu, X. Q. Zhu, Y. J. Pang, Z. H. Shen, Q. Wu, S. Y. Fu and H. Chen, *Chem. Eng. J.*, 2021, **413**, 127502.
6 X. Y. Deng, J. J. Li, Z. Shan, J. W. Sha, L. Y. Ma, N. Q. Zhao and J. Mater, *Chem. A*, 2020, **8**, 11617–11625.
7 Y. Liu and L. J. Wu, *Nano Energy*, 2023, **109**, 108290.
8 Z. X. Xu, R. J. Ma and X. L. Wang, *Energy Storage Mater.*, 2022, **46**, 233–242.
9 M. Sevilla, N. Díez and A. B. Fuertes, *ChemSusChem*, 2021, **14**, 94–117.
10 M. Yuan, T. C. Liu, Q. Shi and J. X. Dong, *Chem. Eng. J.*, 2022, **428**, 132016.
11 C.-C. Hou, Y. Wang, L. Zou, M. Wang, H. Liu, Z. Liu, H.-F. Wang, C. Li and Q. Xu, *Adv. Mater.*, 2021, **33**, 210698.
12 W. Na, J. Jun, J. W. Park, G. Lee, J. Jang and J. Mater, *Chem. A*, 2017, **5**, 17379–17387.

13 X. Liu, J. Rahmatinejad and Z. Ye, *Chem. Eng. J.*, 2021, **422**, 130129.
14 X. Liu, M. M. Vadiyar, J. K. Oh and Z. Ye, *ACS Appl. Mater. Interfaces*, 2021, **13**(28), 32916–32929.
15 L. Zhang, X. Qiu, S. Yang, S. Sun, L. Chen and W. Zhang, *Energy Storage Mater.*, 2023, **61**, 102887.
16 M. Cao, Y. Shu, Q. Bai, C. Li, B. Chen, Y. Shen and H. Uyama, *Sci. Total Environ.*, 2023, **884**, 163750.
17 P. Jessop, *Green Chem.*, 2020, **22**, 13.
18 L. Wang, M. Peng, J. Chen, X. Tang, L. Li, T. Hu, K. Yuan and Y. Chen, *ACS Nano*, 2022, **16**, 2877–2888.
19 Z. Xu, Z. Sun, J. Shan, S. Jin, J. Cui, Z. Deng, M. H. Seo and X. Wang, *Adv. Funct. Mater.*, 2023, **34**, 2302818.
20 Y. Zhang, F. Deng, Q. Zhang, Y. Li, Y. Li, J. Shang, J. Wang, R. Gao and R. Li, *J. Energy Storage*, 2023, **73**, 109098.
21 L. Zhao, S. Sun, J. Lin, L. Zhong, L. Chen, J. Guo, J. Yin, H. N. Alshareef, X. Qiu and W. Zhang, *Nano-Micro Lett.*, 2023, **15**, 41.
22 L. Huang, Y. Xiang, M. Luo, Q. Zhang, H. Zhu, K. Shi and S. Zhu, *Carbon*, 2021, **185**, 1–8.
23 W. J. Chen, C. X. Zhao, B. Q. Li, T. Q. Yuan and Q. Zhang, *Green Chem.*, 2022, **24**, 565–584.
24 R. Madhu, A. P. Periasamy, P. Schlee, S. Hérou and M.-M. Titirici, *Carbon*, 2023, **207**, 172–197.
25 G. Nazir, A. Rehman, S. Hussain, Q. Mahmood, M. Fteiti, K. Heo, M. Ikramf and M. A. Ud Din, *Green Chem.*, 2023, **25**, 4941–4980.
26 N. Guo, M. Li, X. K. Sun, F. Wang and R. Yang, *Green Chem.*, 2017, **19**, 2595–2602.
27 P. Bai, Y. W. He, X. X. Zou, X. X. Zhao, P. X. Xiong and Y. H. Xu, *Adv. Energy Mater.*, 2018, **8**, 1703217.
28 H. Y. Liu, H. S. Chen, K. Y. Shi, F. Zhang, S. W. Xiao, L. Q. Huang and H. Zhu, *Ind. Crops Prod.*, 2022, **187**, 115519.
29 J. Wang, J. Polleux, J. Lim and B. Dunn, *J. Phys. Chem. C*, 2007, **111**, 14925–14931.
30 S. T. Zhang, J. H. Xiao, G. Wang and G. Chen, *Bioresour. Technol.*, 2020, **304**, 122975.
31 S. G. Kostryukov, H. B. Matyakubov, Y. Y. Masterova, A. S. Kozlov, M. K. Pryanichnikova, A. A. Pynenkov and N. A. Khluchina, *J. Anal. Chem.*, 2023, **78**, 718–727.
32 J. Lehto, J. Louhelainen, T. Kłosińska, M. Drożdżek and R. Alén, *Biomass Convers. Biorefin.*, 2018, **8**, 847–855.
33 H. X. Zhu, Q. L. Ma, J. Sheng and R. D. Yang, *Green Chem.*, 2020, **22**, 942–949.
34 A. K. Chandel, F. A. F. Antunes, V. Anjos, M. J. V. Bell, L. N. Rodrigues, I. Polikarpov, E. R. de Azevedo, O. D. Bernardinelli, C. A. Rosa, F. C. Pagnocca and S. S. da Silva, *Biotechnol. Biofuels*, 2014, **7**, 63.
35 W. L. Zhang, J. Yin, C. W. Wang, L. Zhao, W. B. Jian, K. Lu, H. B. Lin, X. Q. Qiu and H. N. Alshareef, *Small Methods*, 2021, **5**, 2100896.
36 J. Deng, T. Y. Xiong, H. Y. Wang, A. M. Zheng and Y. Wang, *ACS Sustainable Chem. Eng.*, 2016, **4**, 3750–3756.
37 L. Q. Huang, Z. B. Ye and R. Berry, *ACS Sustainable Chem. Eng.*, 2016, **4**, 4937–4950.
38 V. Patil, S. Adhikari, P. Cross and H. Jahromi, *Renewable Sustainable Energy Rev.*, 2020, **133**, 110359.
39 D. Y. Chen, K. H. Cen, X. Z. Zhuang, Z. Y. Gan, J. B. Zhou, Y. M. Zhang and H. Zhang, *Combust. Flame*, 2022, **242**, 112142.
40 Y. J. Meng, C. I. Contescu, P. Z. Liu, S. Q. Wang, S.-H. Lee, J. J. Guo and T. M. Young, *Wood Sci. Technol.*, 2021, **55**, 587–606.
41 K. X. Zou, Y. F. Deng, J. P. Chen, Y. Q. Qian, Y. W. Yang, Y. W. Li, G. H. Chen and J. Power, *Sources*, 2018, **378**, 579–588.
42 H. Wang, M. Wang and Y. B. Tang, *Energy Storage Mater.*, 2018, **13**, 1–7.
43 Z. M. Zou, X. L. Luo, L. Wang, Y. Zhang, Z. J. Xu and C. H. Jiang, *J. Energy Storage*, 2021, **44**, 103385.
44 P. G. Liu, Y. Gao, Y. Y. Tan, W. F. Liu, Y. P. Huang, J. Yan and K. Y. Liu, *Nano Res.*, 2019, **12**, 2835–2841.
45 Y. Li, W. Yang, W. Yang, Z. Q. Wang, J. H. Rong, G. X. Wang, C. J. Xu, F. Y. Kang and L. B. Dong, *Nano-Micro Lett.*, 2021, **13**, 95.
46 Z. R. Lin, H.-Y. Shi, L. Lin, X. P. Yang, W. L. Wu and X. Q. Sun, *Nat. Commun.*, 2021, **12**, 4424.
47 Z. X. Xu, M. Li, W. Y. Sun, T. Tang, J. Lu and X. L. Wang, *Adv. Mater.*, 2022, **34**, 2200077.
48 X. R. Gan, J. Tang, X. Y. Wang, L. Gong, I. Zhitomirsky, L. Qie and K. Y. Shi, *Energy Storage Mater.*, 2023, **59**, 102769.
49 L. Q. Huang, Z. Y. Luo, M. W. Luo, Q. Zhang, H. Zhu, K. Y. Shi and S. P. Zhu, *J. Energy Storage*, 2021, **38**, 102509.